Dalton Transactions

ROYAL SOCIETY OF CHEMISTRY

PAPER

View Article Online
View Journal | View Issue

Cite this: *Dalton Trans.*, 2026, **55**, 4792

A series of Cu*X* (*X* = Br and I) units bearing Ba-MOFs: structures, fluorescence and sensing properties

Can Peng,[a,b,c] Sheng-Mao Zhang,[b] Jin-Mei Liu,[a,b,c] Nian-Hao Wang,[b] Lin-Xu Tian,[a,b,c] Xue-Hao Ping,[a,b,c] Jia-Jing Zhao,[b,c] Zhao-Feng Wu *[b,d] and Xiao-Ying Huang *[b,c]

As one of the alkaline earth metal ions with high coordination numbers, the barium ion (Ba^{2+}) typically shows versatile coordination modes when coordinating with organic ligands to construct metal–organic frameworks (MOFs) featuring novel structural attributes. In this work, based on the diverse coordination modes between Ba^{2+} and isonicotinic acid (HINA) or its derivatives, three MOFs, namely, $Ba_2(Cu_2Br_2)(3\text{-F-INA})_4(H_2O)$ (**1**, 3-F-INAH = 3-fluoroisonicotinate acid), $Ba_2(H_2O)_7Cu_4Br_3(INA)_5$ (**2**) and $Ba_2K_5(DMF)_3[Cu_7I_6(INA)_{10}](H_2O)_{3.5}$ (**3**), with novel structural features are synthesized and characterized. In these compounds, Cu*X* (*X* = Br and I) participates in the assembly reaction *via* coordination with the pyridine N atom of the isonicotinate ligand, featuring one-dimensional (1D) chain-like architectures that are incorporated into the resultant 3D MOFs. Significantly, by varying the substituent groups on HINA and altering the halogen species, the luminescent properties of the as-synthesized MOFs could be tuned. Notably, compound **3** exhibits a bright orange emission and demonstrates a selective fluorescence (FL) quenching response toward the sulfur-containing small molecule cysteine (Cys), highlighting its potential utility in FL-based biomolecular sensing. Furthermore, **3** displays sensitive FL sensing toward Fe^{3+} ions. This study represents the first report on Ba-Cu*X*-INA frameworks exhibiting FL sensing properties, thereby providing a valuable foundation for the development of novel FL Cu*X*-based MOFs for sensing applications.

Received 12th December 2025,
Accepted 20th February 2026

DOI: 10.1039/d5dt02972d

rsc.li/dalton

1. Introduction

Metal–organic frameworks (MOFs), as classic fluorescence (FL) materials, have demonstrated significant potential in sensing applications.[1–4] This is attributed to their tunable structural properties and diverse luminescent characteristics, which enable selective and sensitive responses to specific analytes.[5–7] It is well established that the FL in MOFs can be derived from a variety of sources, including rare-earth (RE) ions,[8] organic ligands,[9] and metal–organic energy transfer processes.[10] Nevertheless, the development of novel FL units for the construction of MOFs aimed at sensing applications remains highly desirable, given the limited availability of RE metals and the inherent challenges associated with the synthesis of organic emitters.[11–13]

On the other hand, inorganic–organic hybrid materials based on Cu*X* (where *X* = Cl, Br, and particularly I) have garnered significant interest due to their FL applications.[14,15] For instance, the research team led by Jing Li presented $Cu_xI_y(L)_z$ (where L denotes organic ligands) hybrid materials that demonstrate particular utility as phosphors in the fabrication of light-emitting diodes (LEDs).[16–18] Apparently, Cu*X* units exhibit remarkable diversity in composition, structure, and fluorescence (FL) properties, while their structural characteristics, anionic species (X^-), and types of organic ligands significantly influence the FL performance of Cu*X*-based hybrid materials. This not only offers ample opportunities for the modulation of their FL properties but also renders Cu*X* units ideal candidates for efficient emissive centers in the construction of FL materials, particularly fluorescent metal–organic frameworks (FL MOFs).[19–21]

Recent studies have demonstrated that MOFs can serve as structural platforms to encapsulate functional inorganic units within their porous architectures, as they can provide abundant coordination sites in the resulting structures.[22–25] Notably, these coordination sites, alongside the diverse coordi-

[a]*College of Chemistry, Fuzhou University, Fuzhou, Fujian, 350108, China*
[b]*State Key Laboratory of Structural Chemistry, Fujian Institute of Research on the Structure of Matter, the Chinese Academy of Sciences, Fuzhou, Fujian, 350108, China. E-mail: zfwu@fjirsm.ac.cn, xyhuang@fjirsm.ac.cn*
[c]*Fujian College, University of Chinese Academy of Sciences, Fuzhou, Fujian, 350002, China*
[d]*Beijing Institute of Graphic Communication, No. 1 (band-2) Xinghua Street, Daxing District, Beijing, 102600, China*

nation modes between metal ions and organic linkers, further confer enhanced structural diversity to the integrated inorganic units within a three-dimensional (3D) porous network.[26–29] Considering this, herein, a series of novel 3D MOFs formulated as $Ba_2(Cu_2Br_2)(3\text{-F-INA})_4(H_2O)$ (**1**, 3-F-INAH = 3-fluoroisonicotinic acid), $Ba_2(H_2O)_7Cu_4Br_3(INA)_5$ (**2**, HINA = isonicotinic acid) and $Ba_2K_5(DMF)_3[Cu_7I_6(INA)_{10}](H_2O)_{3.5}$ (**3**, DMF = *N*,*N*-dimethylformamide), were synthesized and characterized. Based on the diverse coordination modes exhibited between Ba^{2+} ions and INA ligands, Cu*X* (*X* = Br and I) can be engineered into one-dimensional (1D) chain-like architectures and subsequently encapsulated within the resulting MOFs. The FL properties of the title compounds can be modulated through the modification of the substituent groups on HINA and by varying the halogen species. Consequently, compound **3** with 1D $[Cu_7I_6(INA)_{10}]_n^{9n-}$ chains as luminescent centers exhibits a bright orange emission. Moreover, it demonstrates a pronounced FL quenching response to cysteine and Fe^{3+} ions. The underlying sensing mechanism was investigated through a series of comprehensive characterizations. This study is anticipated to provide novel insights into the design of FL sensing MOFs through the incorporation of emissive Cu*X* units.

2. Experimental

2.1 Materials and methods

Detailed information on the materials employed can be found in the SI. Single-crystal X-ray diffraction data were collected with a Rigaku XtaLAB Synergy-R (Mo*K*α, λ = 0.71073 Å) single-crystal diffractometer at 100 K or 280 K. Powder X-ray diffraction (PXRD) patterns were recorded on a Rigaku MiniFlex II diffractometer using Cu*K*α radiation (λ = 1.54178 Å). A graphite monochromator was used and the generator power settings were set at 30 kV and 15 mA. Data were collected in the 2θ range of 5°–50° at a scanning speed of 0.5° min^{-1}. Thermogravimetric analysis (TGA) was performed under a nitrogen atmosphere with a NETZSCH STA449C instrument at a heating rate of 10 °C min^{-1}. Variable-temperature FL spectra were performed on an FLS1000 spectrometer. Energy dispersive spectroscopy (EDS) and scanning electron microscopy (SEM) mapping was observed on a Zeiss Sigma 300 scanning electron microscope with an accelerating voltage of 3 kV. X-ray photoelectron spectroscopy (XPS) was performed on a Thermo Scientific ESCALAB 250 Xi with a monochromatic Al*K*α X-ray source (1486.6 eV) operating at 15 kV and substrate pressure of 5.0×10^{-8} Pa. All peaks were corrected with the characteristic peaks of C 1s (binding energy 284.8 eV), and the peak fittings were analysed using the Avantage 5.932 software.

2.2 X-ray crystallography

Single crystals of the as-made compounds suitable for single-crystal X-ray diffraction (SCXRD) were selected under an optical microscope and glued to a thin glass fiber. The SCXRD data for compounds **1–3** were all collected on a Rigaku XtaLAB Synergy-R single-crystal diffractometer (Mo*K*α radiation, λ = 0.71073 Å), with the data for compound **1** acquired at 280 K and that for compounds **2** and **3** at 100 K, respectively. The structures were solved by direct methods and refined with full-matrix least squares techniques using the SHELX2018 or SHELX2019 package. In compound **1**, one of the crystallographically unique Cu atoms was dealt with as disordered over two positions (Cu(1) and Cu(1B) with an SOF of 0.856(3) and 0.144(3), respectively). It is somewhat unusual that Cu(1B) and the INA ring show a high degree of non-coplanarity. However, it was not possible to sensibly model the ring as disordered due to the low occupancy of the second part. Thus, discussions on the geometry are limited to the main part of the molecule. In addition, one of the 3-F-INA ligands presents disorder in the terminal F/H atoms (F(2)/H(10A) and F(2B)/H(8A) with SOF of 0.432(7) and 0.568(7), respectively). In compound **3**, highly disordered DMF and H_2O molecules are present, and thus soft restraints such as SIMU, SADI, FLAT and ISOR were applied to them to obtain reasonable models. Notably, it was difficult to determine unambiguously the ratio and position of one of the DMF molecules (O12 to C36) and H_2O (O1W to O7W); thus, their SOFs were fixed. The atomic displacement parameters (ADPs) in this region are larger than ideal and in the current model the occupancies of the sites where DMF or water are located do not add up to 1. It is also possible that the disordered K (K(1) and K(1B)) is actually a K/Ba mixture refining to occupancies of approximately 0.95/0.05. Consequently, this section of the molecule is not discussed in detail. Having been well determined and freely refined, the rest of the structure constitutes the focus of our interest and discussion and thus included herein. However, it should be noted that the exact composition in that region has not been unambiguously determined. The final formulae of these structures were determined based on the SCXRD results and EA and TGA characterization. The CCDC numbers are 2504604–2504606, respectively. The crystallographic data and structural refinement details are listed in Table S1. The bond lengths and hydrogen bonding data are listed in Tables S2–7.

2.3 Synthetic procedures

Preparation of compound 1. A mixture of 0.075 g (0.287 mmol) $Ba(NO_3)_2$, 0.10 g (0.448 mmol) $CuBr_2$, 0.10 g (0.602 mmol) KI, 0.10 g (0.523 mmol) 3-fluoroisonicotinic acid (3-F-INAH), 3.0 mL DMF, 2.0 mL CH_3CN and 2.0 mL ethanol was sealed in an 8 mL glass vessel, heated at 100 °C for 4 days, and then cooled to room temperature. The red bulk crystals were selected by hand, washed with absolute ethanol, and then dried in the air.

Preparation of compound 2. A mixture of 0.261 g (1.16 mmol) BaC_2O_4, 0.223 g (1.00 mmol) $CuBr_2$, 0.246 g (2.00 mmol) HINA, and 7.0 mL H_2O was sealed in a 20 mL autoclave, heated at 170 °C for 5 days, and then cooled to room temperature. The yellow rod-like crystals were selected by hand, washed with absolute ethanol, and then dried in the air.

Preparation of compound 3. A mixture of 0.075 g (0.287 mmol) $Ba(NO_3)_2$, 0.10 g (0.525 mmol) CuI, 0.10 g

(0.523 mmol) KI, 0.10 g (0.812 mmol) HINA, 3.0 mL DMF, 2.0 mL CH_3CN, and 2.0 mL ethanol was sealed in an 8 mL glass vessel, heated at 100 °C for 3 days, and then cooled to room temperature. The orange bulk crystals were selected by hand, washed with absolute ethanol, and then dried in the air.

2.4 FL sensing measurements

The as-synthesized crystalline sample of **3** was manually ground to afford a fine powder. Then, the fluorescence of the powder was measured by dispersing 2 mg sample in 2 mL of ethanol (EtOH), methanol (MeOH), ethyl acetate (EtOAc), ethylene glycol (EG), dimethyl sulfoxide (DMSO), acetonitrile (MeCN), *N*,*N*-dimethyl formamide (DMF), and *N*,*N*-dimethyl acetamide (DMA). After ultrasonic treatment, the suspension was placed in a quartz cell of 1 cm-width for FL detection. Detailed detections for all titrants were carried out using a pipette to gradually add DMSO, various 1.0×10^{-2} mol L^{-1} ethanol solutions of amino acids, and 1.0×10^{-3} mol L^{-1} ethanol solution of Fe^{3+} into the FL emulsion of compound **3**. The suspension was transferred into a dry 1 cm-path length quartz cuvette for FL spectroscopy measurement using a HORIBA FluoroMax+ spectrofluorometer, with the system shaken well prior to scanning. For FL detection, the excitation wavelength was set at 465 nm, both the excitation and emission slits were fixed at 5 nm, and the emission spectrum was scanned in the range of 500–780 nm at a scanning speed of 1000 nm min^{-1} with data intervals of 1 nm. Throughout the measurement process, the detection chamber was maintained at a constant temperature of 25 ± 0.5 °C and protected from light.

3. Results and discussion

3.1 Crystal structure description

The SCXRD analysis reveals that compound **1** crystallizes in the orthorhombic system, space group *Pbcm* (Table S1). Its asymmetric unit corresponds to half a formula unit, containing one crystallographically independent Ba^{2+} ion, two Cu^{+} and Br^{-} ions (all in 4*d* special positions), two 3-F-INA^{-} ligands, and half a water molecule (O(1 W) in 4*c* site) that coordinates to the Ba^{2+} ion (Fig. S1). The $Ba(1)^{2+}$ ion exhibits a nine-coordinated geometry, wherein the carboxyl groups from four distinct 3-F-INA^{-} ligands coordinate in a monodentate mode, and the other two carboxyl groups coordinate with a bidentate chelating mode. The neighboring Ba^{2+} ions are interconnected through the bridging oxygen atoms from two monodentate carboxylate groups and one water molecule to form a 1D $[Ba_2(COO)_8(H_2O)]_n^{4n-}$ chain (Fig. 1a). The 1D chains are interconnected by the COO^{-} groups to connect the neighboring ones to generate a 2D network denoted as $\{Ba_2(COO)_4(H_2O)\}_n$ (Fig. 1b). Meanwhile, the Cu^{+} ions are stabilized in a tetrahedral environment, coordinated by two Br^{-} ions and two oxygen from two 3-F-INA^{-} ligands to form a 1D $\{Cu_2Br_2\}_n$ chain (Fig. 1c and S2 and 3). Then, these 1D $\{Cu_2Br_2\}_n$ chains and 2D $\{Ba_2(COO)_4(H_2O)\}_n$ networks are bridged by 3-F-INA^{-} ligands to form the 3D framework of $Ba_2(Cu_2Br_2)(3\text{-F-INA})_4(H_2O)$ (Fig. 1d and S4).

Compound **2** crystallizes in the triclinic system, space group $P\bar{1}$ (Table S1). Its asymmetric unit contains one complete formula unit (Fig. S5). In **2**, each Ba^{2+} ion adopts an eight-coordinate geometry, with the coordination involving two carboxylate groups that bind in either a monodentate or bidentate mode, while the remaining coordination positions are fulfilled by water molecules (Fig. 2a and Table S4). Specifically, the neighboring Ba^{2+} ions are interconnected by sharing a single carboxylate oxygen atom along with two coordinated water molecules, resulting in the formation of a 1D chain-like SBU denoted as $\{Ba_2(COO)_5(H_2O)_7\}_n^{n-}$ (Fig. 2a). In compound **2**, the Cu atoms display two distinct coordination environments: Cu(1) is two-coordinated by two nitrogen atoms originating from two INA^{-} ligands, whereas Cu(2), Cu(3), and Cu(4) are four-coordinated by one nitrogen atom and three bromine atoms, generating a 1D $\{Cu_4Br_3\}_n^{n+}$ chain-like structure (Fig. 2b and

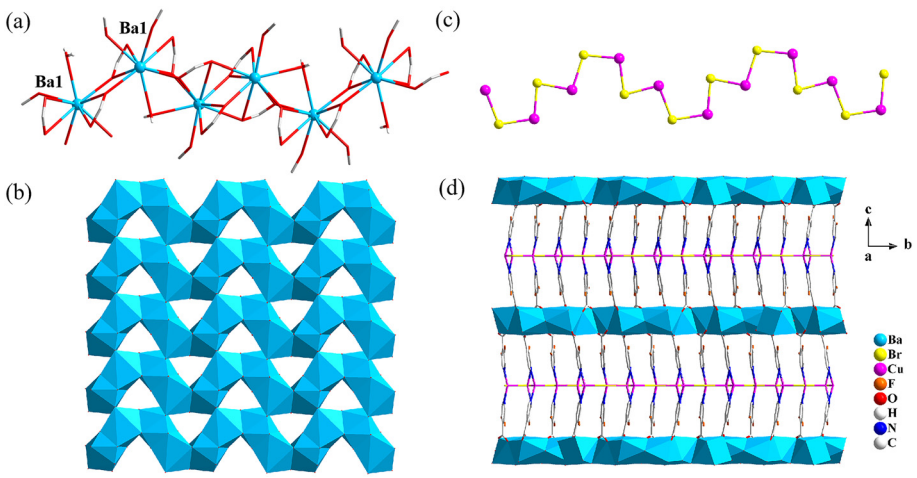

Fig. 1 Crystal structure of compound **1**. (a) 1D $[Ba_2(COO)_8(H_2O)]_n^{4n-}$ chain featuring the coordination environment of the Ba^{2+} ions. (b) 2D $\{Ba_2(COO)_4(H_2O)\}_n$ layered network. (c) 1D $\{Cu_2Br_2\}_n$ chain. (d) 3D framework of compound **1** viewed along the *a*-axis.

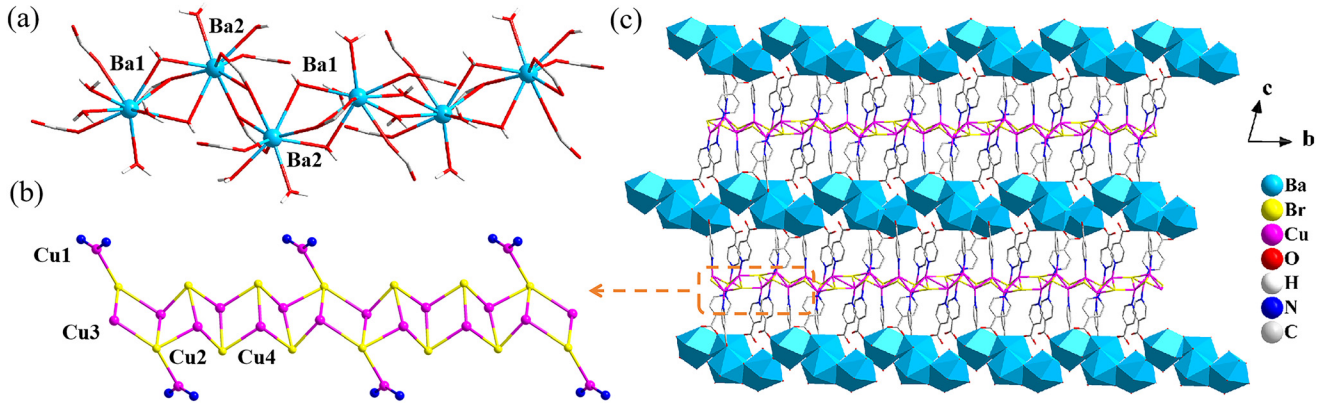

Fig. 2 Crystal structure of compound **2**. (a) 1D $\{Ba_2(COO)_5(H_2O)_7\}_n^{n-}$ chain with the coordination environment of the Ba^{2+} ions. (b) 1D $\{Cu_4Br_3\}_n^{n+}$ chain. (c) 3D framework of compound **2** viewed along the *a*-axis.

S6). The 1D $\{Cu_4Br_3\}_n^{n+}$ chains are bridged with the 1D $\{Ba_2(COO)_5(H_2O)_7\}_n^{n-}$ chains through the INA^- ligands to form a 3D framework (Fig. 2c and S7, 8).

Compound **3** crystallizes in the triclinic system, space group $P\bar{1}$ (Table S1). Its asymmetric unit corresponds to half a formula unit (Fig. S9). In contrast to compounds **1** and **2**, the

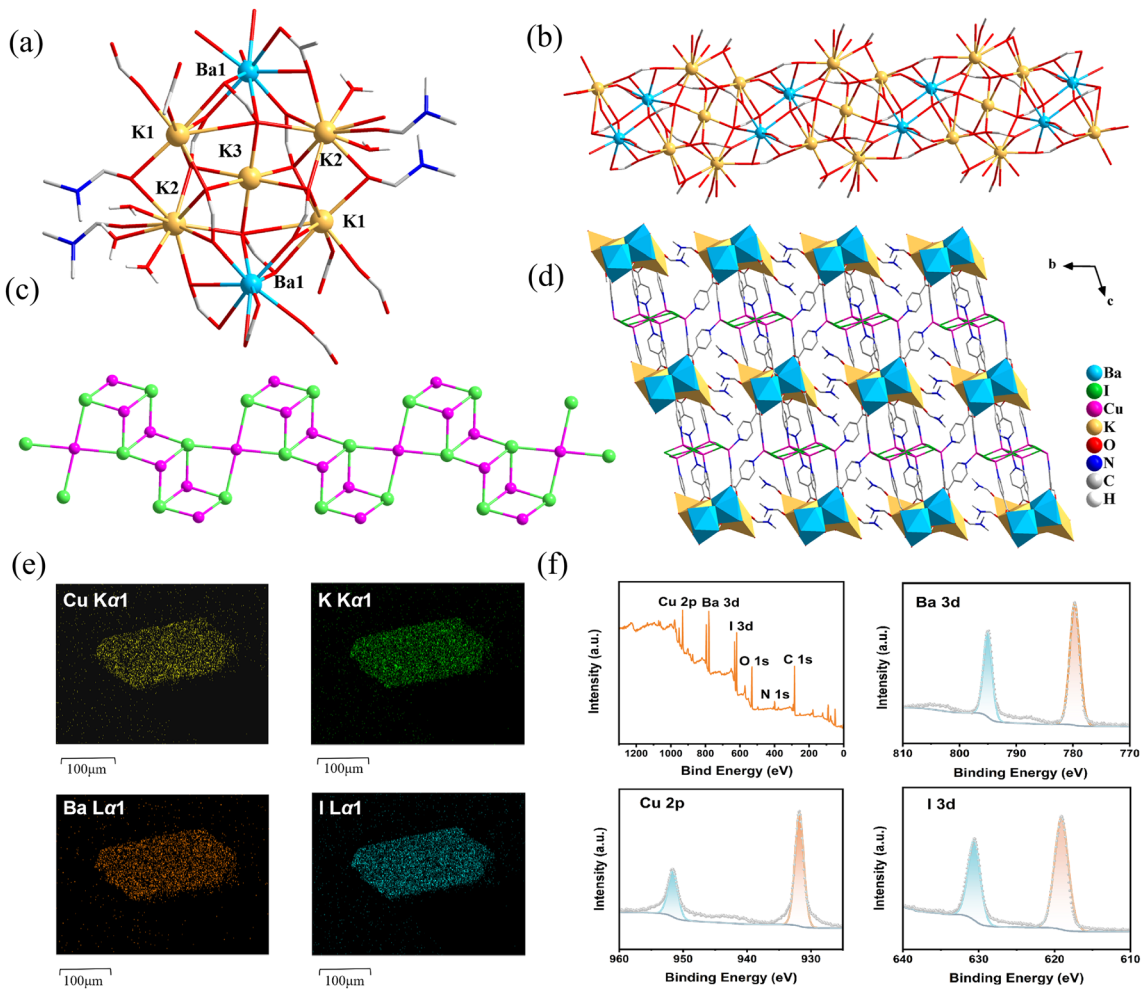

Fig. 3 Crystal structure of compound **3**. (a) Coordination environments of Ba^{2+} and K^+ ions in compound **3**. (b) 1D chain-like structure of $\{Ba_2(COO)_{10}K_5(DMF)_4\}_n^{n-}$. (c) 1D $\{Cu_7I_6\}_n^{n+}$ chain in **3**. (d) 3D framework of compound **3** viewed along the *a*-axis. (e) Elemental mapping images of Ba, K, Cu, and I for compound **3**. (f) XPS survey scan and high-resolution spectra of Cu 2p, I 3d, and Ba 3d for compound **3**.

incorporation of the heterometal K^+ in compound **3** significantly alters the coordination environment of Ba^{2+}. In the crystal structure of compound **3**, Ba^{2+} adopts a nine-coordinate coordination mode, with its coordination environment detailed as follows: the carboxyl groups of three distinct INA^- ligands occupy six coordination sites through a bidentate coordination mode, while the remaining three coordination sites are complemented by three different ligands *via* a monodentate coordination mode. Meanwhile, the K^+ ions exhibit diverse coordination geometries, adopting octa-coordinate, deca-coordinate, and hexa-coordinate configurations, respectively. Specifically, the central K^+ ion is hexa-coordinated by six oxygen atoms from six different carboxylic groups in a monocoordinated way, which is further surrounded by four K^+ ions and two Ba^{2+} ions to form a heptyl-nuclear cluster as an SBU (Fig. 3a). The heptyl-nuclear cluster is further bridged with two neighboring SBUs to assemble into a 1D chain-like $\{Ba_2(COO)_{10}K_5(DMF)_3\}_n^{n-}$ (Fig. 3b). Benefiting from the unique coordination space confinement space constructed by the aforementioned 1D chains and INA^- ligands (Fig. S10), Cu_xI_y SBU in compound **3** features a 1D $\{Cu_7I_6\}_n^{n+}$ chain-like structure (Fig. 3c). The $\{Cu_7I_6\}_n^{n+}$ chains and the $\{Ba_2(COO)_{10}K_5(DMF)_3\}_n^{n-}$ chains are bridged *via* the nitrogen atoms (N) of the pyridine ring in the INA^- ligands to form a novel 3D structure (Fig. 3d and S11).

The phase purity of the as-made compounds was confirmed by comparing the experimental powder X-ray diffractograms (PXRD) with the simulated pattern generated from single-crystal diffraction data (Fig. S12–14, respectively). TG measurements were also conducted to study their thermal properties (Fig. S15–17, respectively). According to the thermogravimetric (TG) curves shown in Fig. S15–17, respectively, compound **1** remains stable up to 200 °C but loses its crystalline water at approximately 215 °C. Following this, its structure undergoes thermal decomposition between 250 °C and 400 °C. Compound **2** demonstrates similar thermal stability to compound **1**, maintaining its structure up to around 200 °C before collapsing due to the removal of its organic components. In the case of compound **3**, a continuous slight weight loss occurs in the range of 50–330 °C, which is attributed to the removal of the solvents DMF and H_2O. Then, rapid weight loss occurs after 330 °C, resulting from its structural collapse.

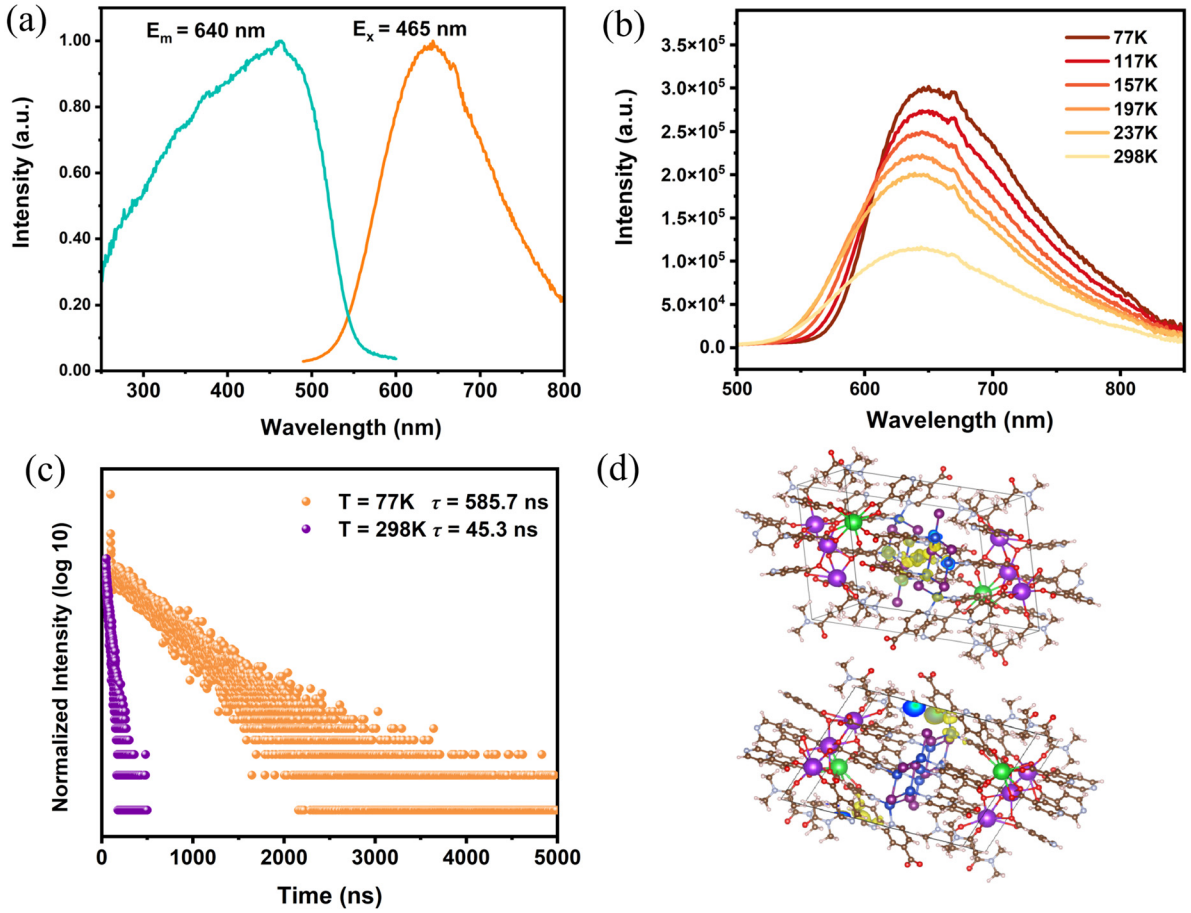

Fig. 4 (a) Excitation and emission spectra of the as-synthesized compound **3**. (b) Temperature-dependent fluorescence spectra of the as-synthesized compound **3** under 465 nm excitation. (c) Time-resolved fluorescence decay curves of compound **3** under 450 nm excitation at 77 K and 298 K (τ = lifetime). (d) Plots of the highest occupied crystal orbital in the VB (top section) and lowest unoccupied crystal orbital in the CB (bottom section) of compound **3**.

Taking compound **3** with diverse components as a case study, the results obtained from EDS and SEM mapping confirm the presence and uniform distribution of the primary elemental constituents (Cu, I, Ba, and K) throughout the crystal specimen (Fig. 3e). These observations are consistent with the XPS data, which identified characteristic orbital signals corresponding to Ba 3d, Cu 2p, and I 3d, respectively. Importantly, the binding energy analysis of the Cu 2p orbital indicates the oxidation state of Cu(I) with no detectable satellite peaks associated with Cu(II) species (Fig. 3f). This result aligns with the structural data derived from the SCXRD and elemental analysis. The SEM mapping measurements of the other compounds are also listed in the SI (Fig. S18 and 19).

3.2 Luminescence properties

At room temperature, compound **1** exhibited no emission upon excitation with ultraviolet light, whereas **2** displayed a weak yellow emission. This difference can be attributed to the presence of the fluorine substituent possessing an electron-withdrawing effect derived from 3-F-INA in **1**. The high electronegativity of fluorine significantly modulates the ligand electronic structure, reducing the π electron cloud density of the aromatic ring and weakening the probability of radiative transition related to ligand-to-metal charge transfer (LMCT) between the ligand and the Cu(I) center, causing the non-emissive character of compound **1**.[30–32]

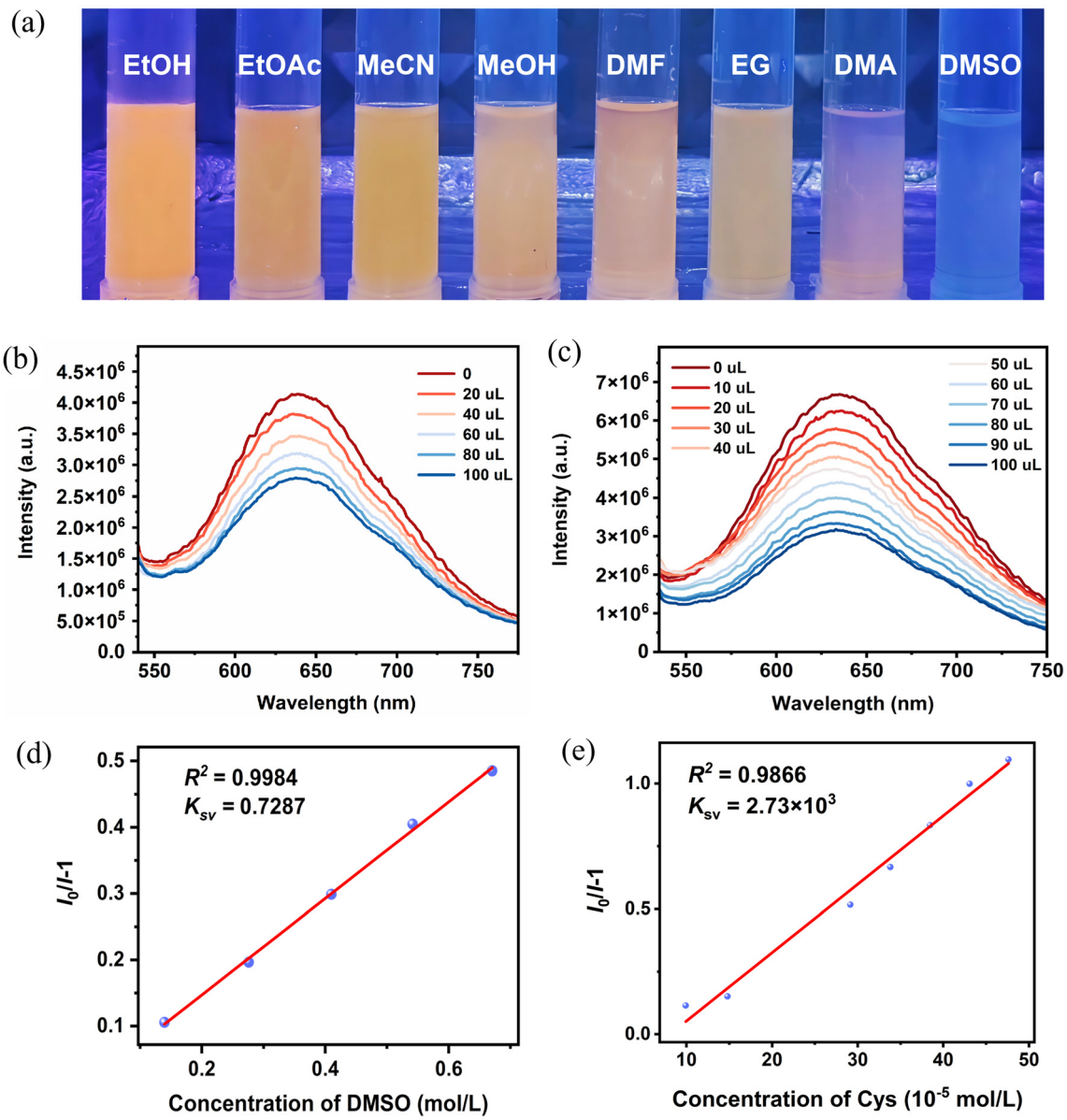

Fig. 5 (a) Photographs of FL emulsions of **3** dispersed in different solvents under 365 nm UV light. (b) FL spectra of **3** upon the addition of different amounts of DMSO. (c) FL spectra of **3** upon the addition of different amounts of 10^{-2} mol L^{-1} Cys. (d) K_{sv} curve for the detection of DMSO. (e) K_{sv} curve for the detection of Cys.

Compound **3**, which contains 1D CuI chains, displays a bright orange FL with a maximum emission peak at 640 nm when excited with 465 nm ultraviolet light (Fig. 4a). Variable-temperature FL spectroscopy shows that its FL intensity slowly diminishes as the temperature gradually increases from 77 to 298 K (Fig. 4b). The FL lifetime characterization indicates that its FL lifetime is 585.7 ns at 77 K, which is nearly thirteen-times greater than that measured at 298 K (Fig. 4c). This result is consistent with other $Cu_xI_y(L)_z$ hybrids exhibiting thermally activated delayed FL (TADF), which can be explained by the decrease in the thermally induced nonradiative decay process.[33–36] A similar phenomenon has also been observed for compound **2** (Fig. S20–22). DFT calculations showed that the valence band (VB; top section) and conduction band (CB; bottom section) of compound **3** originate from its CuI component and the INA^- ligand, respectively (Fig. 4d). These findings suggest that its emission predominantly arises from energy transfer between its 1D $[Cu_7I_6]_n^{n+}$ chains and INA^- ligands, which serve as the principal FL center within **3**.[32,37]

3.3 FL sensing properties

The as-prepared crystals of compound **3** were ground into a powder and dispersed in organic solvents regularly used in the lab to evaluate their FL sensing capacities. As illustrated in Fig. 5a and S23, compound **3** exhibits a pronounced and selective FL quenching response to DMSO. Upon the addition of DMSO into the FL emulsion of compound **3**, its FL intensity is quenched gradually (Fig. 5b). This result highlights its potential utility for the selective detection of sulfur-containing compounds. As is known, cysteine, a crucial sulfur-containing biomolecule, plays a significant role in biological systems, and alterations in its concentration are closely linked to a range of pathological conditions.[38–40] Consequently, the development of sensitive methods for the detection of cysteine is of considerable importance. As seen in Fig. 5c, by dispersing compound **3** in 2 mL of ethanol with varying volumes of 10^{-2} mol L^{-1} cysteine, the FL intensity decreases gradually with the addition of cysteine in an incremental way. To quantitatively analyze the FL quenching effect of DMSO and Cys, the Stern–Volmer (SV) equation of $I_0/I = 1 + K_{sv} \times [M]$ was employed, where I_0 represents the FL intensity of **3** without the quenching analyte, I is the FL intensity after adding the quencher, $[M]$ is the concentration of the quencher and K_{sv} is the quenching constant.[41] As depicted in Fig. 5d and e, the SV plot showed a good linear relationship with a high R^2 value, and the calculated quenching constant was 0.7287 L mol^{-1} and 2.73×10^3 L mol^{-1}, respectively. The sensing performances for Cys are comparable to other FL MOFs based on ligand modification and

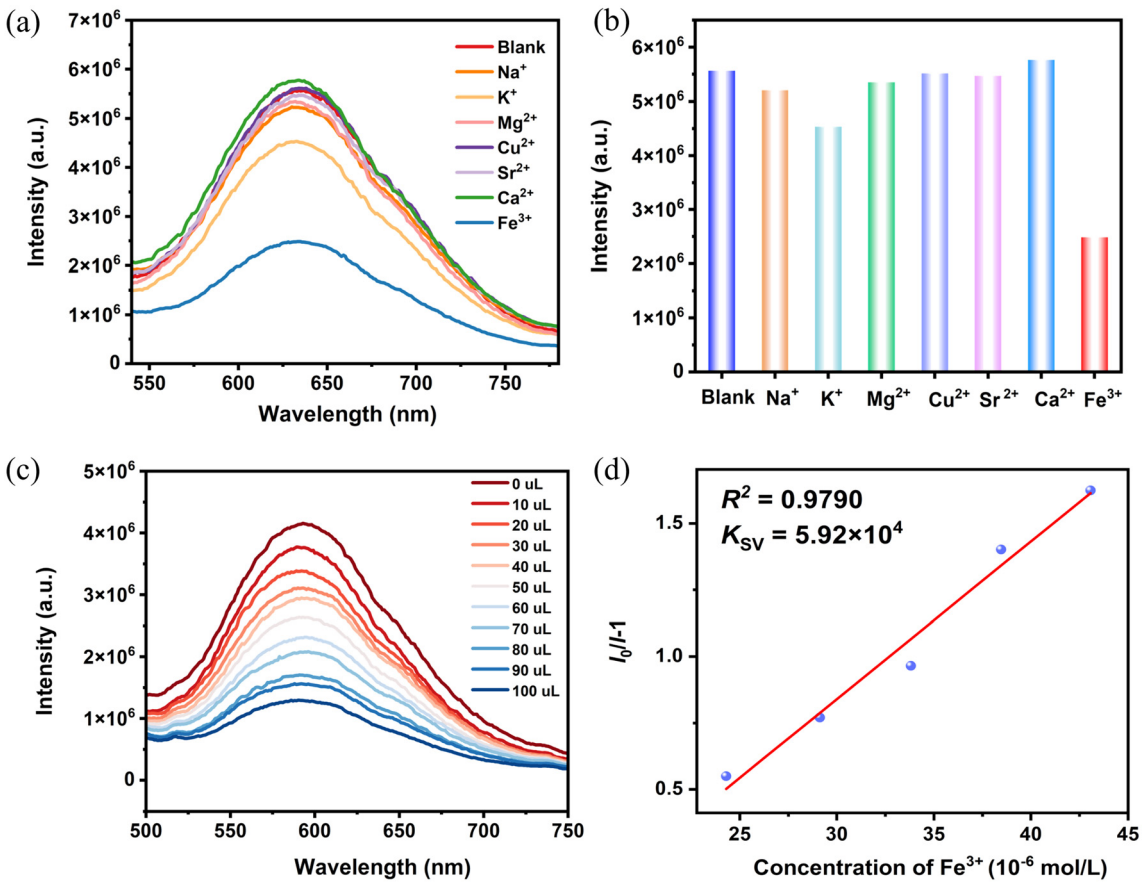

Fig. 6 (a) Comparison of the FL intensities of compound **3** dispersed in various 10^{-2} mol L^{-1} metal ions. (b) FL intensities of compound **3** towards various 10^{-2} mol L^{-1} metal ions. (c) FL spectra of **3** upon the addition of different amounts of 10^{-3} mol L^{-1} Fe^{3+}. (d) K_{sv} curve for the detection of Fe^{3+}.

constructed from rare-earth metals (Table S8).[42–46] Other sulfur-containing amino molecules also showed some degree of quenching effect on the fluorescence of compound **3**, while the amino acids without sulfur showed almost no quenching effect, as shown in Fig. S24. By contrast, compound **3** exhibited the strongest quenching response to Cys, demonstrating its selective sensing.

Compound **3** was dispersed in a series of 10^{-2} mol L^{-1} ethanol solutions of metal nitrates (M = Na^+, K^+, Mg^{2+}, Ca^{2+}, Cu^{2+}, Sr^{2+}, and Fe^{3+}) to investigate its potential FL sensing of metal ions. As shown in Fig. 6a and b, compound **3** exhibits a significant selective quenching effect toward Fe^{3+} in contrast to the other metal ions under the same measuring conditions. As seen in Fig. 6c, with the addition of 10^{-3} mol L^{-1} Fe^{3+} into the FL emulsion, the FL intensity of compound **3** was quenched gradually. The quenching percentage exceeded 50% when only 50 μL of 10^{-3} mol L^{-1} Fe^{3+} was added, demonstrating its sensing sensitivity. As shown in Fig. 6d, the SV plot shows a good linear relationship (R^2 = 0.9790), and the calculated quenching constant, K_{sv} is calculated to be 5.92×10^4 L mol^{-1}.[47,48] Its sensing performances are better than that of other FL MOFs constructed from rare metals and FL ligands, indicating that the CuI module could be a good candidate as an FL sensing module to build FL MOFs (Table S8).[49–52] The FL sensing response of compound **3** to both Cys and Fe^{3+} ions indicates that the CuX units are promising building blocks and emissive units to construct FL MOFs.

In Cys, its thiol (–SH) group as a nucleophilic donor can form strong coordinate bonds with the electrophilic Cu(I) sites in the 1D $\{Cu_7I_6\}_n^{n+}$ chains.[53,54] As shown in Fig. S25, the EDS mapping analysis revealed a uniform distribution of sulfur in the sample following the sensing tests, confirming the strong interaction between cysteine and compound **3**. XPS analysis indicated no significant shifts in the positions or shapes of the Cu(I) 2p and I 3d characteristic peaks, confirming the chemical stability of the 1D $\{Cu_7I_6\}_n^{n+}$ chains throughout the sensing (Fig. S26). The weak signal of the S 2p characteristic peak further demonstrated the specific coordination between Cys and surface-exposed Cu(I) sites *via* thiol groups. Based on the above-mentioned characterization, the thiol group (–SH) in Cys as a typical nucleophilic donor specifically coordinates with the electrophilic Cu(I) sites on the 1D $\{Cu_7I_6\}_n^{n+}$ chains in **3**, and the local electronic microenvironment of the 1D CuI chains as the emission center for the compound is altered, which induces FL quenching.[55]

4. Conclusions

In conclusion, three FL Ba-CuX-INA (X = Br and I) MOFs were synthesized *via* the solvothermal method. By taking advantage of the diverse coordination properties between Ba^{2+} and the isonicotinate ligand or its derivative, CuX could be tuned into 1D chain-like units and confined into the 3D crystal lattice of the title three MOFs. Notably, through monitoring the functional groups in the organic ligand and the halide ions, compound **3** exhibits bright orange luminescence and showed specific FL quenching responses toward Cys and Fe^{3+} with high selectivity and sensitivity. This study presents an important reference towards the design of novel FL MOFs by using CuX units as promising emissive and building blocks.

Author contributions

Can Peng: data curation, writing original draft, writing – reviewing and editing, validation, investigation and software. Sheng-Mao Zhang: software, visualization. Jin-Mei Liu: data curation, software and formal analysis. Nian-Hao Wang: methodology. Lin-Xu Tian: data curation, validation. Xue-Hao Ping: validation and investigation. Jia-Jing Zhao: validation and investigation. Zhao-Feng Wu: conceptualization, writing, reviewing and editing, funding acquisition, resources, visualization, supervision, and project administration. Xiao-Ying Huang: reviewing and editing, writing, reviewing and editing, conceptualization, resources, visualization, supervision, and project administration.

Conflicts of interest

There are no conflicts to declare.

Data availability

The data that support the findings of the study are included in main text and supplementary information (SI). Supplementary information: PXRD patterns, more crystal structural details, PL spectra, TG curve, *etc*. See DOI: https://doi.org/10.1039/d5dt02972d.

Raw data can be obtained from the corresponding author upon request. Source data are provided with this paper.

CCDC 2504604–2504606 contain the supplementary crystallographic data for this paper.[56a–c]

Acknowledgements

This research was funded by the National Natural Science Foundation of China (No. 22175178).

References

1 L. E. Kreno, K. Leong, O. K. Farha, M. Allendorf, R. P. Van Duyne and J. T. Hupp, *Chem. Rev.*, 2011, **112**, 1105–1125.
2 Z. Hu, B. J. Deibert and J. Li, *Chem. Soc. Rev.*, 2014, **43**, 5815–5840.
3 H.-Y. Li, S.-N. Zhao, S.-Q. Zang and J. Li, *Chem. Soc. Rev.*, 2020, **49**, 6364–6401.
4 J. Zhou, Y. Li, W. Wang, X. Tan, Z. Lu and H. Han, *Biosens. Bioelectron.*, 2020, **164**, 112332.

5 P. Horcajada, R. Gref, T. Baati, P. K. Allan, G. Maurin, P. Couvreur, G. Férey, R. E. Morris and C. Serre, *Chem. Rev.*, 2011, **112**, 1232–1268.
6 W. P. Lustig, S. Mukherjee, N. D. Rudd, A. V. Desai, J. Li and S. K. Ghosh, *Chem. Soc. Rev.*, 2017, **46**, 3242–3285.
7 Y. Cai, T. Dong, Z. Bian, H. Liu, X. Liu and A. Liu, *Coord. Chem. Rev.*, 2025, **529**, 216470.
8 J. Rocha, L. D. Carlos, F. A. A. Paz and D. Ananias, *Chem. Soc. Rev.*, 2011, **40**, 926–940.
9 W. Lu, Z. Wei, Z.-Y. Gu, T.-F. Liu, J. Park, J. Park, J. Tian, M. Zhang, Q. Zhang, T. Gentle III, M. Bosch and H.-C. Zhou, *Chem. Soc. Rev.*, 2014, **43**, 5561–5593.
10 B. Li, H. M. Wen, Y. Cui, W. Zhou, G. Qian and B. Chen, *Adv. Mater.*, 2016, **28**, 8819–8860.
11 C.-X. Yao, N. Zhao, J.-C. Liu, L.-J. Chen, J.-M. Liu, G.-Z. Fang and S. Wang, *Polymers*, 2020, **12**, 691.
12 N. Wu, C. Bo and S. Guo, *ACS Sens.*, 2024, **9**, 4402–4424.
13 Z. W. Jiang, X. Gong, P. Zhang and Y. Wang, *TrAC, Trends Anal. Chem.*, 2025, **184**, 118133.
14 L. Boivin and P. D. Harvey, *J. Mater. Chem. C*, 2024, **12**, 14253–14282.
15 J. Jiang, Z.-W. Li, Z.-Z. Zhang, B. Tan, Z.-F. Wu and X.-Y. Huang, *Dalton Trans.*, 2024, **53**, 706–714.
16 W. Liu, Y. Fang, G. Z. Wei, S. J. Teat, K. Xiong, Z. Hu, W. P. Lustig and J. Li, *J. Am. Chem. Soc.*, 2015, **137**, 9400–9408.
17 W. Liu, Y. Fang and J. Li, *Adv. Funct. Mater.*, 2018, **28**, 1705593.
18 Y. Fang, C. A. Sojdak, G. Dey, S. J. Teat, M. X. Li, M. Cotlet, K. Zhu, W. Liu, L. Wang, D. M. ÓCarroll and J. Li, *Chem. Sci.*, 2019, **10**, 5363–5372.
19 M. S. Deshmukh, A. Yadav, R. Pant and R. Boomishankar, *Inorg. Chem.*, 2015, **54**, 1337–1345.
20 J. Jeong, Y. Choi and J.-H. Cha, *ACS Appl. Nano Mater.*, 2025, **8**, 14759–14766.
21 N. H. Wang, K. Zhao, B. Tan, Z. F. Wu, X. Y. Huang and J. Li, *Adv. Opt. Mater.*, 2025, **13**, e01516.
22 G. Li, S. Zhao, Y. Zhang and Z. Tang, *Adv. Mater.*, 2018, **30**, 1800702.
23 X. Wang, Y. Wang and Y. Ying, *TrAC, Trends Anal. Chem.*, 2021, **143**, 116395.
24 Y. Ghahramani, N. Hajipour, O. Tavakkol, M. Gholami, M. Yari Kalashgrani, V. R. Neralla, W.-H. Chiang and S. M. Mousavi, *Chem. Rec.*, 2025, e202500146.
25 T. L. Easun, F. Moreau, Y. Yan, S. Yang and M. Schröder, *Chem. Soc. Rev.*, 2017, **46**, 239–274.
26 S. L. Griffin and N. R. Champness, *Coord. Chem. Rev.*, 2020, **414**, 213295.
27 H. Wu, W. Zheng, R. Zhu, M. Zhou, X. Ren, Y. Wang, C. Cheng, H. Zhou and S. Cao, *Chem. Eng. J.*, 2023, **452**, 139475.
28 W. Ki, X. Z. Hei, H. T. Yi, W. Liu, S. J. Teat, M. J. Li, Y. Fang, V. Podzorov, E. Garfunkel and J. Li, *Chem. Mater.*, 2021, **33**, 5317–5325.
29 J. Troyano, F. Zamora and S. Delgado, *Chem. Soc. Rev.*, 2021, **50**, 4606–4628.
30 J. Sadhukhan, M. Mukherjee, P. Chatterjee and A. Datta, *ACS Omega*, 2025, **10**, 7389–7399.
31 M. Morita, S. Yamada and T. Konno, *Molecules*, 2021, **26**, 2274.
32 K. Hassanein, J. Conesa-Egea, S. Delgado, O. Castillo, S. Benmansour, J. I. Martínez, G. Abellán, C. J. Gómez-García, F. Zamora and P. Amo-Ochoa, *Chem. – Eur. J.*, 2015, **21**, 17282–17292.
33 Y. Song, R. Fan, P. Wang, X. Wang, S. Gao, X. Du, Y. Yang and T. Luan, *J. Mater. Chem. C*, 2015, **3**, 6249–6259.
34 R. Czerwieniec, M. J. Leitl, H. H. H. Homeier and H. Yersin, *Coord. Chem. Rev.*, 2016, **325**, 2–28.
35 X. Hei, W. Liu, K. Zhu, S. J. Teat, S. Jensen, M. Li, D. M. ÓCarroll, K. Wei, K. Tan, M. Cotlet, T. Thonhauser and J. Li, *J. Am. Chem. Soc.*, 2020, **142**, 4242–4253.
36 K. H. Song, J. J. Wang, L. Z. Feng, F. He, Y. C. Yin, J. N. Yang, Y. H. Song, Q. Zhang, X. C. Ru, Y. F. Lan, G. Zhang and H. B. Yao, *Angew. Chem., Int. Ed.*, 2022, **61**, e202208960.
37 Z.-F. Wu, C. Wang, X. Liu, K. Tan, Z. Fu, S. J. Teat, Z.-W. Li, X. Hei, X.-Y. Huang, G. Xu and J. Li, *J. Am. Chem. Soc.*, 2023, **145**, 19293–19302.
38 S. Zhang, C.-N. Ong and H.-M. Shen, *Cancer Lett.*, 2004, **208**, 143–153.
39 H. S. Jung, X. Chen, J. S. Kim and J. Yoon, *Chem. Soc. Rev.*, 2013, **42**, 6019–6031.
40 B. D. Paul, J. I. Sbodio and S. H. Snyder, *Trends Pharmacol. Sci.*, 2018, **39**, 513–524.
41 J. Keizer, *J. Am. Chem. Soc.*, 1983, **105**, 1494–1498.
42 Y.-A. Li, C.-W. Zhao, N.-X. Zhu, Q.-K. Liu, G.-J. Chen, J.-B. Liu, X.-D. Zhao, J.-P. Ma, S. Zhang and Y.-B. Dong, *Chem. Commun.*, 2015, **51**, 17672–17675.
43 J. Zhao, Y.-N. Wang, W.-W. Dong, Y.-P. Wu, D.-S. Li and Q.-C. Zhang, *Inorg. Chem.*, 2016, **55**, 3265–3271.
44 Y. Zheng, C. C. Zhang and Q. Wang, *Sens. Actuators, B*, 2017, **245**, 622–640.
45 Z. Wu, H. Xu, W. He, J. Wang, M. Muddassir, X. Liu and Y. Wang, *Talanta*, 2024, **280**, 126715.
46 J. Chai, C. Liu, H. Yang, Y. Han, Y. Liu, Y. Zhang and X. Zhang, *Inorg. Chem.*, 2025, **64**, 9886–9896.
47 J.-S. Shen, D.-H. Li, M.-B. Zhang, J. Zhou, H. Zhang and Y.-B. Jiang, *Langmuir*, 2011, **27**, 481–486.
48 E. Lee, H. Ju, J. H. Jung, M. Ikeda, Y. Habata and S. S. Lee, *Inorg. Chem.*, 2019, **58**, 1177–1183.
49 M. Zheng, H. Tan, Z. Xie, L. Zhang, X. Jing and Z. Sun, *ACS Appl. Mater. Interfaces*, 2013, **5**, 1078–1083.
50 F. Zhao, X.-Y. Guo, Z.-P. Dong, Z.-L. Liu and Y.-Q. Wang, *Dalton Trans.*, 2018, **47**, 8972–8982.
51 Y. Zhao, X. Zhai, L. Shao, L. Li, Y. Liu, X. Zhang, J. Liu, F. Meng and Y. Fu, *J. Mater. Chem. C*, 2021, **9**, 15840–15847.
52 S.-R. Zhang, W.-T. Zhang, X. Li, G.-J. Xu, W. Xie, Y.-H. Xu, N. Xu and Z.-M. Su, *Inorg. Chem.*, 2025, **64**, 2990–2999.
53 A. Rigo, A. Corazza, M. L. di Paolo, M. Rossetto, R. Ugolini and M. Scarpa, *J. Inorg. Biochem.*, 2004, **98**, 1495–1501.
54 L.-C. Königsberger, E. Königsberger, G. Hefter and P. M. May, *Dalton Trans.*, 2015, **44**, 20413–20425.

55 Y. Zhao, H. Zeng, X.-W. Zhu, W. Lu and D. Li, *Chem. Soc. Rev.*, 2021, **50**, 4484–4513.
56 (*a*) CCDC 2504604: Experimental Crystal Structure Determination, 2026, DOI: 10.5517/ccdc.csd.cc2q27pr; (*b*) CCDC 2504605: Experimental Crystal Structure Determination, 2026, DOI: 10.5517/ccdc.csd.cc2q27qs; (*c*) CCDC 2504606: Experimental Crystal Structure Determination, 2026, DOI: 10.5517/ccdc.csd.cc2q27rt.